



## Dynamics of floating objects at high particulate Reynolds numbers

H. Ghaffarian 

*Univ Lyon, INSA Lyon, Ecole Centrale de Lyon, Université Claude Bernard Lyon I, CNRS, LMFA,  
UMR 5509, 20 avenue Albert Einstein, F-69621 VILLEURBANNE, France  
and Univ Lyon, UMR 5600, Environnement-Ville-Société CNRS, F-69362 Lyon, France*

D. Lopez  and E. Mignot

*Univ Lyon, INSA Lyon, Ecole Centrale de Lyon, Université Claude Bernard Lyon I, CNRS, LMFA,  
UMR 5509, 20 avenue Albert Einstein, F-69621 VILLEURBANNE, France*

H. Piegay

*Univ Lyon, UMR 5600, Environnement-Ville-Société CNRS, F-69362 Lyon, France*

N. Riviere 

*Univ Lyon, INSA Lyon, Ecole Centrale de Lyon, Université Claude Bernard Lyon I, CNRS, LMFA,  
UMR 5509, 20 avenue Albert Einstein, F-69621 VILLEURBANNE, France*



(Received 20 June 2019; accepted 1 April 2020; published 28 May 2020)

The motion of high Reynolds number objects at free surfaces is a general problem that has many industrial and ecological applications, such as hazard assessment due to driftwood in rivers or motion of plastic patches in the oceans. Modeling such object trajectories in a flow can be done assuming the object to be a tracer or using Newton's second law in the form of the Basset-Boussinesq-Oseen equation. In many studies, however, the latter approach can be difficult to implement due to the presence of complex forces at play and a high computational cost, thus knowing the validity of the tracer model can be very useful for practical applications. In this work, we study theoretically and experimentally the dynamics of high Reynolds number floating objects in one- and two-dimensional free surface flows. We first verify that the two-dimensional surface version of the Basset-Boussinesq-Oseen equation can accurately model floating object trajectories. Following our theoretical analysis, we introduce a characteristic response distance noted  $\lambda$  that scales the acceleration distance of a floating object, and we show that it is about two to four times the body length in the streamwise direction. The dimensionless parameter  $\lambda^*$  obtained by normalizing  $\lambda$  by a flow length scale then plays a role analogous to that of the Stokes number at low particulate Reynolds number. Moreover, we show that once the floating object reaches the flow velocity, or if at any given time its velocity is equal to that of the flow, the floating object behaves like a tracer, regardless of  $\lambda^*$ . These results can greatly simplify the analyses and computations of the motion of floating objects at high particulate Reynolds number, first by identifying a characteristic distance  $\lambda$  scaling the length of the acceleration phase, and then by showing that once the flow velocity is reached, the object is transported as a passive tracer.

DOI: [10.1103/PhysRevFluids.5.054307](https://doi.org/10.1103/PhysRevFluids.5.054307)

---

\*[hossein.ghaffarian@insa-lyon.fr](mailto:hossein.ghaffarian@insa-lyon.fr)

## I. INTRODUCTION

The motion of solid objects under flow is a fundamental problem found in many natural and industrial systems. The particular case of floating objects has important ecological applications: floating plastic waste is infamous for forming plastic continents in oceanic gyres [1], rivers and sewers have to contend with an increasing amount of floating pollutants [2], and floating wood, notably large trunks, can be responsible for damaging hydraulic structures and increasing flood risks due to bridge clogging [3,4]. Actually, the transport and deposition of large wood in urban areas may potentially be a worse hazard than the flood flow itself, in particular due to bridge clogging [5,6]. Note, however, that floating wood is also considered to be a natural phenomenon contributing to the ecological integrity of rivers [7]. Understanding the dynamics of such floating objects can thus help to balance ecological improvements and natural hazards associated with the presence of floating wood in rivers, for instance by optimizing hydraulic structures and retention devices [8]. Recent experimental studies have provided new insights into log jam formation on bridges and bridge piers, showing how clogging decreases with decreasing wood length, increasing flow velocity, and with better pier streamlining [9–11]. The latter point reveals the importance of flow streamlines and large wood motion on log jam occurrence on an obstacle.

The motion of objects floating at the flow surface can be predicted by two different approaches: (i) a “kinematic” approach considering that the object acts as a tracer following the flow, and (ii) a “dynamic” approach based on the forces acting on the object.

On the one hand, in the kinematic approach, it is assumed that, at any point, the object’s velocity is equal to the flow velocity, and the object’s trajectory is consistent with the flow streamlines. This approach is often used in oceanography to simulate transport and accumulation of marine debris, in particular due to its small computational costs, providing consistent results with data extracted from different cleaning operations as benchmarks [12,13]. This approach has also been tested in a recent study on wood motion in rivers [14]. In this study, the authors use a “semitracer” model assuming that the floating pieces of wood have a velocity slightly lower than that of the flow. This model provides good agreement with experiments, showing that this approach is able to predict and simulate patterns of wood motion and deposits. Some observations on the field support this approach, such as Ref. [15], where the authors show that the wood pieces have almost the same velocity as the flow. One can note finally that passive surface tracers are commonly used as a proxy for measuring surface velocities in laboratory experiments [16,17] and in the field [15,18], or to study surface turbulence and passive particle clustering [19,20].

On the other hand, the dynamic approach is based on Newton’s second law and requires us to calculate the forces exerted by the fluid on the object. Such an approach is widely used for describing the motion of particles fully immersed in turbulent flows [21,22], and it relies in the general case on the Basset-Boussinesq-Oseen (BBO) equation, describing the advection of a solid spherical particle in a nonstationary and nonuniform flow [23]. This equation is valid for small particles compared to the flow scales, and it was initially derived at zero particulate Reynolds number, characterizing the ratio between pressure and viscous fluid forces at the particle scale. The BBO equation has been widely used to study particle dynamics, preferential concentration, and settling properties both numerically [21,24,25] and experimentally [26,27]. As the particulate Reynolds number increases, this equation is modified by taking into account nonlinear drag and lift forces. For Reynolds numbers of order 1, Bergougnoux *et al.* [28] showed that the main correction to include in the BBO equation is a modified drag force, using the Schiller-Naumann correlation for the drag coefficient. At larger values of the particulate Reynolds number (up to  $10^3$ ), quadratic expressions for the drag and lift forces provide accurate results [29,30]. These results are not restricted to spherical objects, and several studies have shown that the BBO model equation is indeed valid also for rod- and disklike particles [31–34]. Whereas most studies based on this dynamic approach consider immersed particles (neutrally buoyant or not), only a few apply this approach to the case of objects floating at a free surface. Recently, Persi *et al.* [34,35] showed that a surface version of the BBO equation provides accurate modeling of the same experimental trajectories in a meandering channel flow as those of Ruiz-Villanueva *et al.* [14] discussed above.

This last example raises the question of finding a criterion for the validity of the kinematic approach when the particulate Reynolds number is large (typically above  $10^2$  in the studies mentioned above). Indeed, using this model can be much simpler and faster for calculating object transport, in particular in complex flows that might not be so well captured at small scales, as in oceanography. At a low particulate Reynolds number, a nondimensional ratio between the particle viscous response time and the flow timescale, known as the Stokes number, is usually taken to be the criterion to distinguish between two approaches so that deviations from the kinematic model are expected to occur at moderate and large Stokes numbers. The present work thus aims at analyzing the validity of both approaches in order to provide conditions under which a high Reynolds number floating object would behave as a flow tracer. Using a theoretical approach and an open channel flow experiment, we identify a typical length scale for the distance of acceleration from rest of floating objects, and we then test the influence of this scale compared to the flow length scale on the object's ability to follow the flow. The remainder of the paper is organized as follows. Section II presents the general equation of motion and a theoretical analysis on the validity of the tracer model, followed in Sec. III by the experimental setup. Sections IV and V present our experimental results in a one-dimensional acceleration flow and in a two-dimensional flow past a cylinder, followed finally by a discussion and conclusion in Sec. VI.

## II. DYNAMIC MODEL FOR FLOATING OBJECTS AT LARGE PARTICULATE REYNOLDS NUMBER

We present hereafter the theoretical equation describing the advection of a floating object by a flow. As mentioned in the Introduction, object motion is described in the general case of a nonuniform and unsteady flow by the Basset-Boussinesq-Oseen (BBO) equation for a point object. The complete form of this equation is available both for low particulate Reynolds numbers [23] and high particulate Reynolds numbers [30].

In this study, we focus on the high particulate Reynolds number case, and we consider objects floating at a free surface. Due to the high particulate Reynolds number, the drag force is quadratic with the relative velocity, and the Basset (or history) term is negligible [30]. Furthermore, the condition of buoyancy balance implies that there is no net vertical force on the object and therefore no vertical motion, and it yields an important result that the mass of displaced fluid is equal to the mass of the object. This feature is found similarly in the case of a neutrally buoyant fully immersed particle. Additionally, we focus on cases in which there is no lift force, which can occur, for instance, in a potential flow that has no vorticity and considering objects that are symmetric with respect to the flow. Under these conditions, the advection equation reads

$$m(1 + C_A)\frac{d\mathbf{v}}{dt} = m(1 + C_A)\frac{D\mathbf{u}}{Dt} + \frac{1}{2}\rho_f C_D S |\mathbf{u} - \mathbf{v}|(\mathbf{u} - \mathbf{v}), \quad (1)$$

where  $m = m_p = m_f$  is the mass of the floating object at a free surface (thus that of the displaced fluid),  $\mathbf{v}$  and  $\mathbf{u}$  are the object and fluid velocities,  $\rho_f$  is the fluid density,  $C_A$  and  $C_D$  are the added mass and drag coefficients, and  $S$  is the submerged frontal area of the object;  $\frac{D}{Dt} = \frac{\partial}{\partial t} + \mathbf{u} \cdot \nabla$  is the convective derivative. Note that Eq. (1) is valid for a point object, considering the object size to be much smaller than the typical flow length scale  $L_0$ . Since we consider floating objects similar to wood in rivers, their size is much greater than the capillary length, so that capillary effects can be neglected [36].

This equation can be written in a dimensionless form using the flow quantities  $U_0$  and  $L_0$  as reference velocity and length scales, respectively, so that the reference time scale is  $L_0/U_0$ . Denoting nondimensional quantities with  $*$ , Eq. (1) results in

$$\frac{d\mathbf{v}^*}{dt^*} = \frac{D\mathbf{u}^*}{Dt^*} + \frac{1}{\lambda^*} |\mathbf{u}^* - \mathbf{v}^*|(\mathbf{u}^* - \mathbf{v}^*), \quad (2)$$

where

$$\lambda^* = \frac{\lambda}{L_0} = \left( \frac{2(1 + C_A) V_f}{C_D S} \right) \frac{1}{L_0}, \quad (3)$$

$V_f$  being the displaced fluid volume (or equivalently the object submerged volume). In Eq. (2), the left-hand side is the object dimensionless acceleration, and the right-hand side is the dimensionless fluid forces.

The first term on the right-hand side of Eq. (2), namely  $\frac{D\mathbf{u}^*}{Dt^*}$ , referred to as the undisturbed flow force, is due to viscous stresses and pressure gradients existing within the base flow [37]. It is interesting to note that in the present problem of floating objects, the prefactor of the dimensionless undisturbed flow force is exactly 1, as is the case for fully immersed neutrally buoyant particles.

The second term on the right-hand side of Eq. (2) is the dimensionless drag force, scaled by  $1/\lambda^*$ , where  $\lambda^*$  is a ratio between a length scale  $\lambda$  based on the object characteristics and the flow length scale  $L_0$ . This expression of the drag force is always valid, considering that the drag coefficient is a function of the particulate Reynolds number  $Re_p$ . Note that  $C_A$  can also vary with  $Re_p$  but with a much weaker sensitivity, so that the influence of the  $1 + C_A$  term in Eq. (3) does not play a significant role at leading order. At low  $Re_p$ ,  $C_D$  is inversely proportional to  $Re_p$ , so that this expression of the nondimensional drag force can be simplified and results in the low Reynolds expression  $F_D^* = \frac{1}{St}(\mathbf{u}^* - \mathbf{v}^*)$ , where the Stokes number  $St$  is the ratio between the object viscous response time and the flow timescale, characterizing object inertia [23]. More details about this scaling are provided in Appendix. At large  $Re_p$ , however (typically  $Re_p > 10^2$ ), the specificity is that the drag coefficient  $C_D$  is almost independent of the particulate Reynolds number [38,39]. In that case,  $\lambda^*$  is a fixed ratio between an object-based scale  $\lambda$  and the flow length scale  $L_0$ . One can thus provide an interpretation for  $\lambda^*$  by analogy with the Stokes number, considering  $\lambda$  as the object characteristic response distance, scaling the distance traveled by the object while adapting to the flow. Moreover, since  $C_D$  and  $C_A$  are both of order 1 for such objects when  $Re_p \gg 1$  [40,41], we get from Eq. (3) that  $\lambda$  should be proportional to the ratio between the object submerged volume  $V_f$  and submerged frontal area  $S$ . As a result,  $\lambda$  is expected to scale as the length of the object in the direction of flow, denoted  $L_x$  in the following.

The scaling of the dimensionless drag force by  $\lambda^*$  can provide some insights into a floating object dynamics in the  $\lambda^* \ll 1$  and  $\lambda^* \gg 1$  asymptotic regimes. The case in which  $\lambda^* \ll 1$  results in  $\mathbf{v}^* \approx \mathbf{u}^*$  almost immediately, as the object drag force and therefore acceleration cannot tend to infinity. On the other hand, when  $\lambda^* \gg 1$  the drag force becomes negligible compared to the undisturbed flow force. Since Eq. (2) is valid only for point objects for which object dimensions are much smaller than the flow dimension  $L_0$ , this case actually corresponds to  $C_D \lll 1$ . Due to the prefactor 1 before the undisturbed flow force term, the resulting equation is  $d\mathbf{v}^*/dt^* = D\mathbf{u}^*/Dt^*$ . This yields an interesting result, namely that for an object with  $m_p = m_f$  (either floating or neutrally buoyant), if at a given time  $\mathbf{v}^* = \mathbf{u}^*$ , then for any subsequent time  $\mathbf{v}^* = \mathbf{u}^*$ . Note, however, that  $\lambda^* \gg 1$  implies that the object acceleration will occur on extremely long distances compared to the flow scale.

This asymptotic analysis suggests, therefore, that as soon as  $\mathbf{v}^* = \mathbf{u}^*$ , the point object model predicts a tracer behavior regardless of  $\lambda^*$  (or equivalently the Stokes number at low  $Re_p$ ). We thus address two questions in this paper to validate this analysis. First, is  $\lambda$  a suitable length scale for the acceleration of a large Reynolds number floating object under flow? And, if so, is it proportional to the object streamwise length  $L_x$ ? Second, if initially  $\mathbf{v}^* = \mathbf{u}^*$ , will the object be a tracer regardless of  $\lambda^*$ , i.e., will  $\mathbf{v}^*$  be equal to  $\mathbf{u}^*$  at all times? To address these questions, we designed two sets of experiments described in the next section.

### III. MATERIALS

In this work, we perform two sets of experiments in an open flume with floating disks of various diameters and cylinders of various lengths: (i) object acceleration from rest in a uniform flow, and

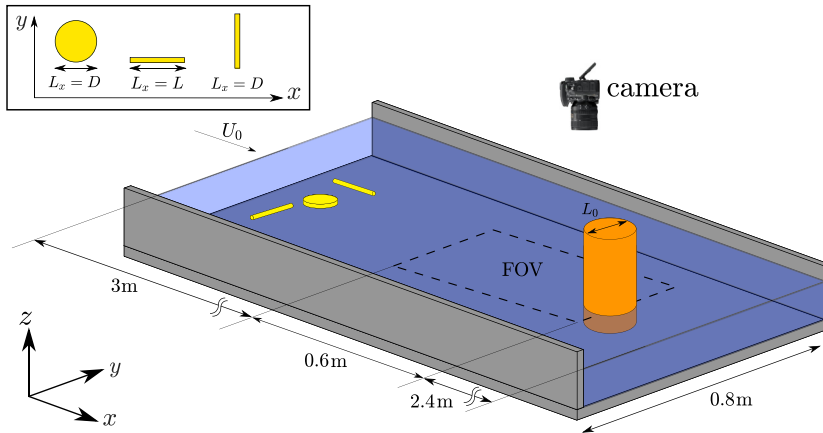


FIG. 1. Schematic view of the experimental setup (not at scale). Note that the obstacle (orange cylinder) is installed only for the second experiment: “motion in a nonuniform flow.”

(ii) object motion in nonuniform flow, considering here a flow passing around a cylinder. To get a correct averaging, the first set of experiments is repeated 25 times and the second part is repeated 100 times for each configuration. To match with our theoretical analysis regarding the absence of lift force, we consider a flow without vorticity, and symmetric floats with respect to the flow direction. Figure 1 shows the schematic design of the experimental setup.

### A. Flume and flow

The experiments are carried out in a straight, rectangular, 6-m-long, 0.8-m-wide flume with a glass bottom and walls. A centrifugal pump immersed in an underground sump provides the discharge in an upstream tank. It is measured with an electromagnetic flow-meter (Promag 50, from Endress-Hausser) with an uncertainty of 0.05 L/s. Perforated plates, a honeycomb, and finally a buffer made of several layers of chicken wire, located in the upstream converging part of the flume, tranquilize, straighten, and homogenize the flow. The channel entrance corresponds to the end of this converging part. Water depths are measured using a point-gauge with an uncertainty of about 0.25 mm. The bottom slope is 0.1 mm/m, and the range of discharge is 16–19 L/s and that of water depth is 105–115 mm, corresponding to hydraulic diameter based Reynolds numbers in the range 80 000–95 000, and the Froude number is about 0.2. Three velocity measurements were implemented to assess the flow homogeneity and uniformity along the flume: (i) micropropeller velocity measurements in the flow bulk, (ii) particle tracking velocimetry (PTV) to check the reproducibility of the same flow characteristics in different tests, showing a relative error of 1%, and (iii) surface particle image velocimetry (SPIV) in the region where the tests were conducted, using small sawdust particles as tracers, to quantify the surface velocity fields. The results show that the flow is steady, uniform, turbulent, and subcritical, and the surface velocity  $U_0$  is typically 20 cm/s.

Based on some preliminary tests, not shown here for the sake of brevity, we observed that as long as the immersed dimension of the object is less than half the flow depth, the object motion is affected only by the surface velocity and not the vertical velocity profile. This condition is largely satisfied in all experiments, so that the object motion is only driven by the two-dimensional surface flow.

### B. Floats

In these experiments we consider two types of objects, namely paraffin disks and wooden cylinders released both aligned and perpendicular to the main flow. The object characteristics

TABLE I. Characteristics of the floating objects used in the experiments.

	$D$ (cm)	$L$ (cm)	$Re_p$	$\rho_p/\rho_f$
Disks (paraffin)	2, 3, 5, 6, 8, 9, 10	1	400 to $10^4$	0.88
Cylinders (wood)	1	1, 2, 3, 5, 10, 15, 20	200 to $10^4$	0.64

are given in Table I, with  $D$  and  $L$  their diameter and length,  $\rho_p/\rho_f$  the relative density, and  $Re_p$  the particulate Reynolds number based on the diameter and minimum slip velocities,  $Re_p = |\mathbf{v} - \mathbf{u}|D/\nu$ , with  $\nu = 10^{-6} \text{ m}^2 \text{ s}^{-1}$  the fluid kinematic viscosity. The experiments on wooden logs were conducted with dry objects. Note that the effect of log wetting during the experiments was checked and did not yield any measurable effect.

Two methods were tested for releasing the objects: (i) using a small bar to hold the object and then suddenly lifting it, and (ii) manually holding and releasing the object. Comparison between the two methods yields the same results within our precision range, thus only the manual method is used in the experiments presented throughout the paper. It should be noted that the control on the object is lost as soon as it starts moving. Sufficiently big objects (longer than 3 cm) keep their initial orientation throughout their trajectory; it is not the case for smaller objects whose orientation is random due to experimental noise. Additionally, most floats are large enough to neglect the capillary effect. As the capillary length is about 1 cm, no clear effect was observed. Note in particular that the contact angle with paraffin is close to  $90^\circ$ , so that even for the smallest disks the capillary forces are expected to remain negligible.

### C. Recording and postprocessing

The surface PIV measurements and object trajectories are recorded using a high spatial resolution camera JAI GO-5000M ( $2560 \times 1700$ ) with 60 Hz frequency. The camera is located above the flume, perpendicular to the flow, 3 m downstream from the channel entrance, with a  $60 \text{ cm} \times 50 \text{ cm}$  field of view (FOV). The time evolution of the object position is determined using a standard image detection algorithm using MATLAB R2017a<sup>®</sup>. The error due to the lack of clarity in pixels is about 2 pixels, which is of the order of 0.1 mm; this is negligible compared to the size of the objects and the object displacement between two consecutive images. The image distortion due to fish-eye was corrected with a standard procedure using MATLAB R2017a<sup>®</sup>, resulting in a remaining bias of less than 0.1 mm, which is again negligible compared to the flow and trajectory scales.

## IV. OBJECT ACCELERATION IN UNIFORM FLOW

In this first experiment, we want to verify if  $\lambda$  is a characteristic response distance, scaling the object acceleration. To address this question, the easiest way is to consider object acceleration from rest in a uniform flow. Assuming a one-dimensional uniform flow of surface velocity  $U_0$  and a constant  $\lambda$  value along the entire trajectory, Eq. (2) has the following analytical solution for  $x(t = 0) = 0$  and  $v(t = 0) = v_0$ :

$$\tilde{x}(\tilde{t}) = \tilde{t} - \ln[1 + (1 - \tilde{v}_0)\tilde{t}], \quad (4)$$

where  $\tilde{x} = \frac{x}{\lambda}$ ,  $\tilde{t} = \frac{t}{\lambda/U_0}$ , and  $\tilde{v}_0 = v_0/U_0$  is the initial velocity. Note that here a tilde denotes a nondimensional variable using  $\lambda$  as a length scale, since there is no characteristic flow length scale in this problem. The assumption of constant  $\lambda$  is valid provided the hydrodynamic coefficients  $C_A$  and  $C_D$  do not vary along the trajectory. This is actually the case for high  $Re_p$  objects, but one has to keep in mind that as the object accelerates,  $Re_p$  decreases.

These acceleration measurements are performed on each floating object and repeated 25 times in order to get a correct averaging. The objects are released in the middle of the channel, 3 m downstream the channel entrance, i.e., at the upstream limit of the FOV, in order to record their



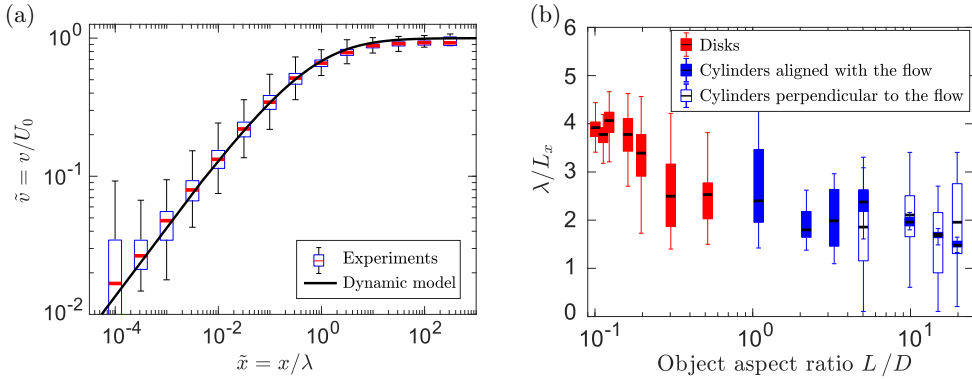


FIG. 2. Object acceleration in a uniform flow: (a) Comparison of the dimensionless velocity as a function of the object’s dimensionless position for all experimental data together (boxplots corresponding to the interquartile and extreme values of all trajectories, with the median shown by a red line) and the solution of the dynamic model from Eq. (4) (black line); (b) evolution of  $\lambda$  normalized by the object’s streamwise body length  $L_x$  for floating disks ( $L_x = D$ , red boxplots), cylinders released aligned with the flow ( $L_x = L$ , filled blue boxplots), and cylinders released perpendicular to the flow ( $L_x = D$ , empty blue boxplots).

1D acceleration from rest. After recording the object acceleration, the initial velocity is measured (since it is experimentally difficult to get an accurate determination of the time at which the motion starts) and Eq. (4) is fitted on the trajectory with a least-squares method using only  $\lambda$  as a calibration parameter [42]. Note that the particulate Reynolds number  $Re_p$  is also calculated along the trajectory in order to check the validity of constant  $\lambda$  assumption, which was the case in all experiments.

### A. Experimental results

In a first step, the model of Eq. (4) is validated against our experiments in Fig. 2(a). This figure shows the normalized object velocity  $\tilde{v} = v/U_0$  as a function of the dimensionless position  $\tilde{x} = x/\lambda$  for all objects with different geometries and sizes. The boxplots represent the median (red lines), interquartile range (blue boxes), and minimum and maximum values (black whiskers) of experimental trajectories. The analytical solution of Eq. (4) is shown by a black line. From Fig. 2(a), we readily see that the model agrees very well with the experiments, allowing us to conclude that  $\lambda$  can be considered as a length scale of the object acceleration. As an indication,  $\lambda$  is the distance needed to accelerate and reach about 70% of the surface velocity.

Based on the scaling analysis of Sec. II,  $\lambda$  is expected to scale as the streamwise body length of the floating object  $L_x$ . This is analyzed in Fig. 2(b), which shows  $\lambda$  normalized by  $L_x$  as a function of the object aspect ratio  $L/D$  for floating disks (red boxplots), cylinders aligned with the flow (filled blue boxplots), and perpendicular to the flow (empty blue boxplots). Boxes and whiskers show the interquartile and extreme ranges for each set of objects.

This figure confirms that for all objects, regardless of shape, size, or orientation,  $\lambda$  scales as  $L_x$  the streamwise body length, as expected from Eq. (3). The exact proportionality coefficient ranges from 2 to 4 for two orders of magnitude in aspect ratio. Strikingly, for cylinders aligned and perpendicular to the flow this scaling is very similar, even though  $L_x$  and the shape with respect to the flow are significantly changed. The slight variations of  $\lambda/L_x$  among different objects can be due to changes in  $C_D$  and  $C_A$ , but at leading order these variations are negligible for  $L/D > 0.3$ . For disks, however, in the range  $0.15 < L/D < 0.3$ ,  $\lambda/L_x$  increases with decreasing aspect ratio, i.e., as the disks become flatter. This can be due to increased friction drag rather than pressure drag, thus changing significantly the drag coefficient. Note that since the orientation of short cylinders is random, only one symbol is plotted in the range  $1 < L/D < 4$ .

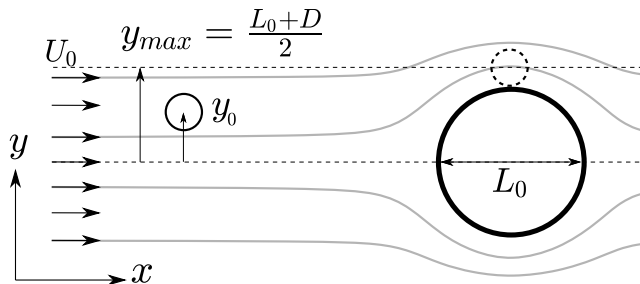


FIG. 3. Schematic view and parameters for the advection experiment in a flow around a cylinder.

In summary, the acceleration experiments show that  $\lambda$  is indeed a characteristic response distance scaling the object response to the flow. For floating objects at large particulate Reynolds number for which the drag and added mass coefficients are expected to be constant and of order 1, this response distance is typically two to four times the streamwise body length, providing a useful tool for estimating this distance with purely geometric information. Once the object reaches the flow velocity, there is still a question of how the object trajectory can be modeled. This is addressed in the next section, where we turn to a nonuniform flow to test the validity of the kinematic and dynamic approaches.

## V. OBJECT MOTION IN A NONUNIFORM FLOW

We consider now an object initially at the flow velocity  $\mathbf{v}^*(t^* = 0) = \mathbf{u}^*$  in a nonuniform flow around a cylinder. This flow is particularly interesting as it can be correctly modeled—apart from the wake—by a 2D potential flow model. Surface PIV was performed and compared to the theoretical expression of the potential flow around a cylinder, showing discrepancies of about 6% in general and up to 12% close to the obstacle. Under this condition, the flow can be considered as irrotational and Eq. (2) can be used to model the advection of objects that are symmetric with respect to the flow.

Figure 3 shows the schematic view of the experiment. An emergent cylinder is located at 3.6 m downstream of the channel entrance, i.e., at the downstream limit of the FOV. This emergent cylinder acts as an obstacle and its diameter can be used as the flow length scale  $L_0$  introduced in Eq. (2). The length of the FOV (60 cm) is chosen so that at the beginning of the FOV the flow is not affected by the obstacle. In this set of experiments, only disks, with seven different diameters  $D = 2, 3, 5, 6, 8, 9,$  and  $10$  cm, are used as floating objects, while three different vertical emergent cylinders placed on the channel bed are used as obstacles ( $L_0 = 4, 10,$  and  $20$  cm), resulting in 21 different  $\lambda^* = \lambda/L_0$  values. To satisfy the initial condition  $\mathbf{v}^* = \mathbf{u}^*$  at the entrance of the FOV, objects are released 3 m upstream of the obstacle, so that at the entrance of the field of view  $v > 0.95U_0$ . The initial lateral position  $y_0$  is varied between the central axis of the obstacle  $y_0 = 0$  and a maximum distance  $y_0 = y_{\max}$ , chosen here to be equal to the sum of the object and obstacle radii  $y_{\max} = (L_0 + D)/2$ . Since the objects are released far upstream, the trajectories are very sensitive to flow perturbations and exhibit a small variability. To overcome this problem, the sampling for each configuration is repeated on average 100 times to get satisfying statistics.

In addition to the experiments, disk trajectories are modeled using Eq. (2), solved numerically using a Runge-Kutta fourth/fifth-order scheme (ode45 in MATLAB<sup>®</sup>). The computations reproduce the experimental trajectories, starting from the experimentally known initial position of the object and its nondimensional response distance  $\lambda^*$  measured in Sec. IV, and using either the theoretical potential flow or the experimentally measured flow.



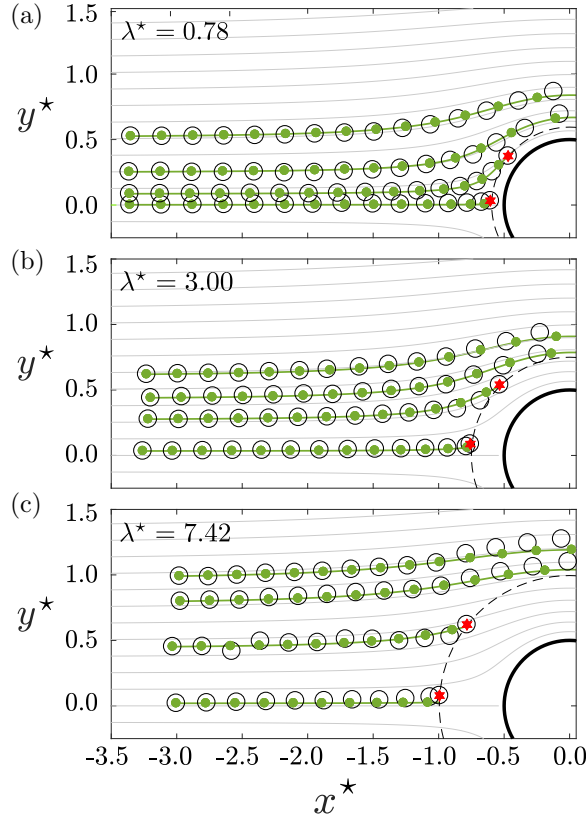


FIG. 4. Comparison between individual experimental trajectories and a numerical model based on the potential flow for  $\lambda^* = 0.78, 3,$  and  $7.42$ . The experimental trajectories are represented as black empty circles, and the dynamic modeled [Eq. (2)] trajectories are represented as green points and solid lines, with the same time step ( $\Delta t^* = 0.47$ ). Note that the symbols are not at scale, and the dashed line around the obstacle represents the limit for impact. Red stars show impacts, and gray lines are flow streamlines.

## Experimental results

### 1. Individual trajectories

We first show some individual trajectories, with and without the impact of the disks to the emergent cylinder. Figure 4 compares the experimental trajectories (black empty circles) with the numerical models (green points and solid line) for three values of  $\lambda^*$ , showing a good agreement between real trajectories and the predictions of the BBO model of Eq. (2). In addition, the model accurately predicts impact occurrence and its location (red stars). An impact is defined only as a contact, and we do not describe the subsequent object motion. Note that the green and black circles only represent the center of mass of floats, and they do not depict at scale the floating disks. In particular, for the highest value of  $\lambda^*$  in Fig. 4(c) the disk diameter is comparable to that of the obstacle, which might call into question the validity of Eq. (2). However, the numerical predictions still show satisfying results, with small deviations observed as the floats pass the cylinder. One can note a slight time lag between experimental and numerical trajectories, due to uncontrolled variations of the surface velocity in the experiments (of less than 2%).

### 2. Statistical analysis

As mentioned previously, each configuration (corresponding to one  $\lambda^*$  value) was repeated on average 100 times, leading to a total of more than 2000 available trajectories. To have a global

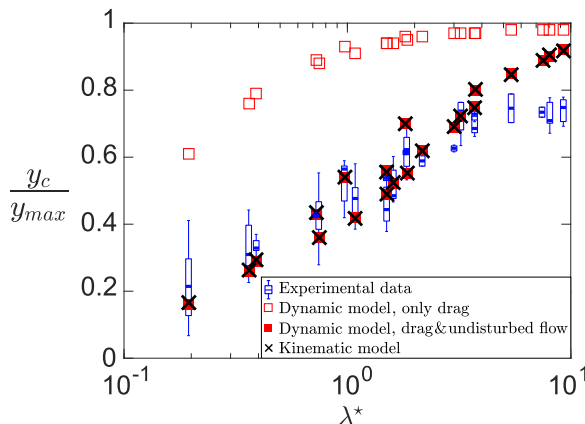


FIG. 5. Critical lateral position for impact  $y_c$  normalized by  $y_{max}$  as a function of  $\lambda^*$ : experiments (blue boxplots), dynamic model of Eq. (2) based on the potential flow using the drag force only (empty red squares) and both forces (filled red squares), and kinematic (i.e., tracer) model (black crosses).

measure of the model validity, we define for each configuration a critical value of the initial lateral position  $y_c$ , so that if  $y_0 \leq y_c$  impact occurs, and if  $y_0 > y_c$  the disk passes the obstacle without impact. Figure 5 shows this distance  $y_c$  normalized by  $y_{max} = (L_0 + D)/2$  as a function of the normalized characteristic response distance  $\lambda^*$ . Due to the experimental variability, for one given  $\lambda^*$  there is a range of  $y_0$  where some objects hit the obstacle and others do not, so  $y_c$  is taken to be the median value of these cases, and the extent of this range is described by the blue boxplots. In this figure, in addition to the experiments, two numerical results are shown, one by considering only the drag force in the BBO equation—so only the second term on the right-hand side of Eq. (2) (empty red squares)—and one considering the full expression of Eq. (2) (filled red squares). Finally, the prediction using the kinematic model ( $\mathbf{v}^* = \mathbf{u}^*$  all along), corresponding to a tracer, is represented by black crosses. Note that this prediction can be obtained analytically from the potential flow streamline equations.

While considering only the drag force is not satisfying, the complete model of Eq. (2) with both undisturbed flow force and drag force predicts the critical lateral position for impact quite accurately (with discrepancies of about 5%). Additionally, the kinematic model provides also very satisfying predictions. The increase in  $y_c/y_{max}$  with  $\lambda^*$  is thus not related to increasing inertia of the floating object. Actually when considering a disk, increasing  $\lambda^*$  can only be achieved by increasing its diameter [see Fig. 2(b)] or decreasing the obstacle diameter, resulting in an increase of  $y_c/y_{max}$  due only to geometry. Moreover, because in Fig. 2(b)  $\lambda/L_x$  is not a bijective function of object geometry, this causes dispersion in the numerical models in Fig. 5. These results confirm the analysis performed in Sec. II that if the floating object is initially at the flow velocity ( $\mathbf{v}^* = \mathbf{u}^*$ ), it behaves as a tracer regardless of its nondimensional response distance  $\lambda^*$ . Note that for large values of  $\lambda^*$ , a deviation is observed between the experimental data and the models. This is again due to the fact that for these large values, the object size is larger than the flow scale  $L_0$ , and the assumption of a point object is clearly broken.

The numerical simulations were also carried out using the experimentally measured velocity field, resulting in very similar results to those shown in Fig. 5 (about a 7% difference on average). Moreover, the assumption of irrotational flow was tested by adding the lift force due to vorticity [30] in these numerical simulations. The simulations on the real flow field with and without lift force due to vorticity give identical results (less than a 4% difference), confirming the validity of the potential flow assumption and that the effect of the lift force is negligible here. These results are thus not shown here for the sake of brevity.

## VI. CONCLUSIONS

In this study, we considered the dynamics of floating objects at a large particulate Reynolds number in two cases, first during their acceleration at the surface of a uniform flow, and second their motion in a nonuniform flow past a cylinder.

We first show that the dynamic model [Eq. (2)] reproduces fairly the accelerated motion of floating objects. Moreover, the acceleration experiments showed that  $\lambda$ , defined in Eq. (3), is an appropriate scaling for object acceleration from rest in a uniform flow, so that after a distance  $\lambda$  the object reaches about 70% of its terminal velocity. Interestingly, whereas at a low particulate Reynolds number the acceleration is scaled by a response time (through the Stokes number; see Appendix), at a large particulate Reynolds number it is a length scale that characterizes acceleration. Additionally, for all objects considered here, regardless of their shape or size,  $\lambda$  was measured to be about two to four times the streamwise body length. This result is valid provided that  $C_D$  and  $C_A$  are of order 1, which is the case for large floating objects such as wood in rivers [43].

In a second experiment, we considered floating objects initially transported almost at the flow velocity and facing an emergent cylinder to explore nonuniform flow effects. The comparison between experiments, dynamic models, and kinematic models shows that these objects all behave as tracers, regardless of their normalized characteristic response distance  $\lambda^*$ , as long as they remain smaller than the flow scale. This is an important result for the study of floating (or neutrally buoyant) objects that was anticipated by the asymptotic analysis of Sec. II. Indeed, as soon as the object reaches the flow velocity, its motion will be accurately predicted by a kinematic model assuming the object is a flow tracer.

To extend the application of the current study to large-scale ecological and hydraulic problems, several future works are worth considering. First, in line with the approach developed in this paper, the influences of flow vorticity—notably in the presence of shear—and of an asymmetry of the objects would be interesting to complete the tests on the use of the Basset-Boussinesq-Oseen equation for high particulate Reynolds numbers, providing insights into the need for integrating these additional features for accurate trajectory predictions. Moreover, as the impact described in this study is a first step for wood trapping and blockage, these results can provide complementary elements to existing study on wood trapping on bridge piers [9,10]. Returning to the motion of wood in rivers or floating plastics in the ocean, studying the influence of complex object shapes—for example the presence of roots to represent the natural wood elements—is also needed. The effect of roots can actually be described by an increase of the object frontal area, which results in a smaller  $\lambda$  [42,44]. Finally, the asymptotic regime corresponding to very small  $\lambda^*$  is also worth studying as it may correspond to flat floats commonly used as tracers in large-scale particle image velocimetry (LSPIV) or seeds in dispersion problems in geophysical flows [45].

## ACKNOWLEDGMENTS

This work was supported by the LABEX IMU (ANR-10-LABX-0088) of Université de Lyon, within the program “Investissements d’Avenir” (ANR-11-IDEX-0007) operated by the French National Research Agency (ANR). This work was performed within the framework of the EUR H2O’Lyon (ANR-17-EURE-0018) of Université de Lyon, within the program “Investissements d’Avenir” operated by the French National Research Agency (ANR). This work benefited from fruitful discussions with V. Ruiz-Villanueva.

## APPENDIX: LINK BETWEEN STOKES NUMBER AND $\lambda^*$

As mentioned in Sec. II, the nondimensional drag force reads

$$F_D^* = \frac{1}{\lambda^*} |\mathbf{u}^* - \mathbf{v}^*| (\mathbf{u}^* - \mathbf{v}^*), \quad (\text{A1})$$

TABLE II. Drag force expressions in the low and large  $\text{Re}_p$  limits.

	$\text{Re}_p \ll 1$	$\text{Re}_p \gg 1$
$C_D \propto$	$\frac{1}{\text{Re}_p} = \frac{\nu}{D \mathbf{u} - \mathbf{v} }$	Cst
$\lambda^* =$	$\text{St} \mathbf{u}^* - \mathbf{v}^* $	Cst
$F_D^* =$	$\frac{1}{\text{St}}(\mathbf{u}^* - \mathbf{v}^*)$	$\frac{1}{\lambda^*} \mathbf{u}^* - \mathbf{v}^* (\mathbf{u}^* - \mathbf{v}^*)$

where

$$\lambda^* = \frac{\lambda}{L_0} = \left( \frac{2(1 + C_A) V_f}{C_D S} \right) \frac{1}{L_0}. \quad (\text{A2})$$

This expression is valid for all values of  $\text{Re}_p$ , but it can be simplified at low  $\text{Re}_p$  since in that case the drag coefficient is inversely proportional to  $\text{Re}_p$ . Table II summarizes the expressions of  $C_D$ ,  $\lambda^*$ , and  $F_D^*$  in the small and high  $\text{Re}_p$  limits for disks. In that case,  $\text{Re}_p = |\mathbf{v} - \mathbf{u}|D/\nu$  and  $V_f/S \propto D$ , so that the low  $\text{Re}_p$  expressions result in the well-known Stokes drag [23,28], with

$$\text{St} \propto \frac{(1 + C_A)D^2 U_0}{\nu L_0} = \frac{T_p}{T_0}, \quad (\text{A3})$$

where  $T_p$  denotes the object viscous response time, and  $T_0 = L_0/U_0$  is the flow time scale.

As a result, at low particulate Reynolds number  $\text{Re}_p$  the drag force is linear with the relative velocity and scaled by the inverse of a timescale ratio known as the Stokes number, and at large  $\text{Re}_p$  the drag force is quadratic and scaled by the inverse of a lengthscale ratio denoted  $\lambda^*$ .

- 
- [1] M. Cole, P. Lindeque, C. Halsband, and T. S. Galloway, Microplastics as contaminants in the marine environment: A review, *Mar. Pollut. Bull.* **62**, 2588 (2011).
  - [2] J. Gasperi, R. Dris, T. Bonin, V. Rocher, and B. Tassin, Assessment of floating plastic debris in surface water along the Seine River, *Environ. Pollut.* **195**, 163 (2014).
  - [3] D. Bocchiola, M. C. Rulli, and R. Rosso, A flume experiment on the formation of wood jams in rivers, *Water Resour. Res.* **44**, W02408 (2008).
  - [4] P. N. De Cicco, E. Paris, V. Ruiz-Villanueva, L. Solari, and M. Stoffel, In-channel wood-related hazards at bridges: A review, *River Res. Appl.* **34**, 617 (2018).
  - [5] N. S. Lassetre and G. M. Kondolf, Large woody debris in urban stream channels: Redefining the problem, *River Res. Appl.* **28**, 1477 (2012).
  - [6] V. Ruiz-Villanueva, J. M. Bodoque, A. Díez-Herrero, and E. Bladé, Large wood transport as significant influence on flood risk in a mountain village, *Nat. Hazards* **74**, 967 (2014).
  - [7] E. Wohl, N. Kramer, V. Ruiz-Villanueva, D. N. Scott, F. Comiti, A. M. Gurnell, H. Piegay, K. B. Lininger, K. L. Jaeger, D. M. Walters *et al.*, The natural wood regime in rivers, *BioScience* **69**, 259 (2019).
  - [8] V. Ruiz-Villanueva, H. Piégay, A. M. Gurnell, R. A. Marston, and M. Stoffel, Recent advances quantifying the large wood dynamics in river basins: New methods and remaining challenges, *Rev. Geophys.* **54**, 611 (2016).
  - [9] I. Schalko, L. Schmocker, V. Weitbrecht, and R. M. Boes, Laboratory study on wood accumulation probability at bridge piers, *J. Hydraul. Res.* **1** (2019).
  - [10] P. N. De Cicco, E. Paris, and L. Solari, Wood accumulation at bridges: Laboratory experiments on the effect of pier shape, in *Proceedings of the 8th River Flow Congress*, edited by Constantinescu, Garcia, and Hanes (2016), pp. 2341–2345.

- 
- [11] L. Schmocker and W. Hager, Probability of drift blockage at bridge decks, *J. Hydraul. Eng.* **137**, 470 (2011).
- [12] D. Hainbucher, T. Pohlmann, and J. Backhaus, Transport of conservative passive tracers in the North Sea: First results of a circulation and transport model, *Cont. Shelf Res.* **7**, 1161 (1987).
- [13] J. Mansui, A. Molcard, and Y. Ourmieres, Modelling the transport and accumulation of floating marine debris in the Mediterranean basin, *Mar. Pollut. Bull.* **91**, 249 (2015).
- [14] V. Ruiz-Villanueva, E. Bladé, M. Sánchez-Juny, B. Martí-Cardona, A. Díez-Herrero, and J. Bodoque, Two-dimensional numerical modeling of wood transport, *J. Hydroinf.* **16**, 1077 (2014).
- [15] B. J. MacVicar and H. Piégay, Implementation and validation of video monitoring for wood budgeting in a wandering piedmont river, the Ain River (France), *Earth Surf. Proc. Landforms* **37**, 1272 (2012).
- [16] E. A. Meselhe, T. Peeva, and M. Muste, Large scale particle image velocimetry for low velocity and shallow water flows, *J. Hydraul. Eng.* **130**, 937 (2004).
- [17] M. Bieri, J. Jenzer, S. A. Kantoush, and J. L. Boillat, Large scale particle image velocimetry applications for complex free surface flows in river and dam engineering, in *Proceedings of the 33rd IAHR 2009 Congress* (Vancouver, Canada, 2009).
- [18] P. Carbonneau and H. Piégay, *Fluvial Remote Sensing for Science and Management*, 1st ed., edited by P. E. Carbonneau and H. Piégay (John Wiley and Sons, Hoboken, NJ, 2012).
- [19] S. Lovecchio, C. Marchioli, and A. Soldati, Time persistence of floating-particle clusters in free-surface turbulence, *Phys. Rev. E* **88**, 033003 (2013).
- [20] P. Gutiérrez and S. Aumaître, Clustering of floaters on the free surface of a turbulent flow: An experimental study, *Eur. J. Mech. B/Fluids* **60**, 24 (2016).
- [21] F. Toschi and E. Bodenschatz, Lagrangian properties of particles in turbulence, *Annu. Rev. Fluid Mech.* **41**, 375 (2009).
- [22] S. Balachandar and J. K. Eaton, Turbulent dispersed multiphase flow, *Annu. Rev. Fluid Mech.* **42**, 111 (2010).
- [23] M. R. Maxey and J. Riley, Equation of motion for a small rigid sphere in a nonuniform flow, *Phys. Fluids* **26**, 883 (1983).
- [24] M. R. Maxey, The motion of small spherical particles in a cellular flow field, *Phys. Fluids* **30**, 1915 (1987).
- [25] V. Armenio and V. Fiorotto, The importance of the forces acting on particles in turbulent flows, *Phys. Fluids* **13**, 2437 (2001).
- [26] J. R. Fessler, J. D. Kulick, and J. K. Eaton, Preferential concentration of heavy particles in a turbulent channel flow, *Phys. Fluids* **6**, 3742 (1994).
- [27] R. Monchaux, M. Bourgoïn, and A. Cartellier, Analyzing preferential concentration and clustering of inertial particles in turbulence, *Int. J. Multiphase Flow* **40**, 1 (2012).
- [28] L. Bergougnoux, G. Bouchet, D. Lopez, and E. Guazzelli, The motion of solid spherical particles falling in a cellular flow field at low Stokes number, *Phys. Fluids* **26**, 093302 (2014).
- [29] M. S. Howe, On the force and moment on a body in an incompressible fluid, with application to rigid bodies and bubbles at high and low Reynolds numbers, *Q. J. Mech. Appl. Math.* **48**, 401 (1995).
- [30] J. Magnaudet and I. Eames, The motion of high-Reynolds-number bubbles in inhomogeneous flows, *Annu. Rev. Fluid Mech.* **32**, 659 (2000).
- [31] G. A. Voth and A. Soldati, Anisotropic particles in turbulence, *Annu. Rev. Fluid Mech.* **49**, 249 (2017).
- [32] C. Yin, L. Rosendahl, S. K. Kær, and H. Sørensen, Modelling the motion of cylindrical particles in a nonuniform flow, *Chem. Eng. Sci.* **58**, 3489 (2003).
- [33] M. Mandø and L. Rosendahl, On the motion of non-spherical particles at high Reynolds number, *Powder Technol.* **202**, 1 (2010).
- [34] E. Persi, G. Petaccia, and S. Sibilla, Large wood transport modeling by a coupled Eulerian-Lagrangian approach, *Nat. Hazards* **91**, 59 (2018).
- [35] E. Persi, G. Petaccia, S. Sibilla, P. Brufau, and P. García-Navarro, Calibration of a dynamic Eulerian-Lagrangian model for the computation of wood cylinders transport in shallow water flow, *J. Hydroinf.* **21**, 164 (2018).
- [36] P. Singh and D. Joseph, Fluid dynamics of floating particles, *J. Fluid Mech.* **530**, 31 (2005).

- [37] S. E. Corrsin and J. Lumley, On the equation of motion for a particle in turbulent fluid, [Appl. Sci. Res. 6, 114 \(1956\)](#).
- [38] S. F. Hoerner, *Fluid-dynamic Drag: Theoretical, Experimental and Statistical Information* (Hoerner Fluid Dynamics, Vancouver, 1965).
- [39] R. T. Gonçalves, G. R. Franzini, G. F. Rosetti, J. R. Meneghini, and A. L. Fajarra, Flow around circular cylinders with very low aspect ratio, [J. Fluids Struct. 54, 122 \(2015\)](#).
- [40] C. K. Batchelor and G. K. Batchelor, *An Introduction to Fluid Dynamics* (Cambridge University Press, Cambridge, 1967).
- [41] J. W. Bush and I. Eames, Fluid displacement by high Reynolds number bubble motion in a thin gap, [Int. J. Multiphase Flow 24, 411 \(1998\)](#).
- [42] H. Ghaffarian, Study of driftwood dynamics in rivers for hazard assessment, Ph.D. thesis, Univ Lyon, INSA Lyon, 2019.
- [43] C. J. Gippel, I. C. O'Neill, B. L. Finlayson, and I. Schnatz, Hydraulic guidelines for the re-introduction and management of large woody debris in lowland rivers, [Regulated Rivers: Res. Manage. 12, 223 \(1996\)](#).
- [44] H. Ghaffarian, D. Lopez, N. Riviere, H. Piegay, and E. Mignot, Experimental study of the transient motion of floats reproducing floating wood in rivers, in *E3S Web of Conferences* (EDP Sciences, 2018), Vol. 40, p. 02041.
- [45] Q. Rendu, E. Mignot, N. Riviere, B. Lamberti-Raverot, S. Puijalon, and F. Piola, Laboratory investigation of *Fallopia × bohemica* fruits dispersal by watercourses, [Environ. Fluid Mech. 17, 1051 \(2017\)](#).